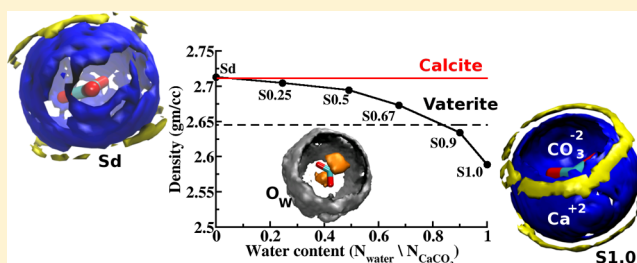


Dehydration-Induced Amorphous Phases of Calcium Carbonate

Moumita Saharay,^{*,†} A. Ozgur Yazaydin,[‡] and R. James Kirkpatrick[¶][†]Department of Chemistry and [¶]College of Natural Science, Michigan State University, East Lansing, Michigan 48824, United States[‡]Department of Chemical Engineering, University of Surrey, Guildford, GU2 7XH, United Kingdom

S Supporting Information

ABSTRACT: Amorphous calcium carbonate (ACC) is a critical transient phase in the inorganic precipitation of CaCO_3 and in biomineralization. The calcium carbonate crystallization pathway is thought to involve dehydration of more hydrated ACC to less hydrated ACC followed by the formation of anhydrous ACC. We present here computational studies of the transition of a hydrated ACC with a $\text{H}_2\text{O}/\text{CaCO}_3$ ratio of 1.0 to anhydrous ACC. During dehydration, ACC undergoes reorganization to a more ordered structure with a significant increase in density. The computed density of anhydrous ACC is similar to that of calcite, the stable crystalline phase. Compared to the crystalline CaCO_3 phases, calcite, vaterite, and aragonite, the computed local structure of anhydrous ACC is most-similar to those of calcite and vaterite, but the overall structure is not well described by either. The strong hydrogen bond interaction between the carbonate ions and water molecules plays a crucial role in stabilizing the less hydrated ACC compositions compared to the more hydrated ones, leading to a progressively increasing hydration energy with decreasing water content.



■ INTRODUCTION

Calcium carbonates are common phases in the natural environment and are important biological materials occurring in, for instance, sea urchins, bivalve shells, earthworms, sponges, and avian eggshells. Calcium carbonates are also widely used in biomimetic materials^{1,2} and are critical in carbon sequestration.^{3–5} There are five crystalline calcium carbonate phases. Calcite, aragonite, and vaterite are anhydrous, whereas ikaite ($\text{CaCO}_3 \cdot 6\text{H}_2\text{O}$) and monohydrocalcite ($\text{CaCO}_3 \cdot \text{H}_2\text{O}$) are hydrous phases. Calcite is the thermodynamically stable anhydrous phase at atmospheric pressure and temperature. In recent years amorphous calcium carbonate (ACC) has been increasingly recognized as an important metastable transitional phase that can lead to the formation of all the anhydrous crystalline polymorphs.^{6–17} Dehydration-induced transformation of ACC to the crystalline forms is important in biomineralization.^{18,19} In this process the energetically descending pathway is thought to involve multiple steps starting with dehydration of a relatively stable hydrous ACC to an anhydrous or less hydrous ACC that readily crystallizes to one of the crystalline phases.^{20,21}

Although recent experimental studies have focused on investigating the role of different hydration states of ACC in biomineralization, there is no consensus regarding the structural changes that occur during dehydration or how these changes can lead to crystallization. For instance, the infrared spectroscopic analysis of stable biogenic ACC extracted from *Pyura pachydermatina* body spicules and *Ficus microcarpa* suggests that short-range ordering around the carbonate groups is similar to that in monohydrocalcite and vaterite.⁶ Extended X-ray absorption fine structure (EXAFS) studies^{22–26} of a

similar biogenic ACC also indicate short-range atomic ordering, at least up to ~ 4 Å. However, the structures of ACCs extracted from different species appear to be different in terms of the local environment around Ca^{2+} , suggesting a more complex situation.⁶ The water loss during the dehydration of ACC has been attributed to the rearrangement of atoms and ions with and without constituent water molecules.^{15,27} ACC dehydration is endothermic, and based on differential scanning calorimetric data, Radha et al.²⁰ have proposed that the enthalpy of dehydration is 40.87 kJ/mol, which is very similar to the heat of vaporization of bulk liquid water.²⁸

Although experimental techniques such as X-ray²³ and neutron scattering²⁹ can provide information about the local radial structure of ACC, determining the extended 3-dimensional arrangement of atoms in noncrystalline materials is difficult, and computational approaches are often used to refine structures obtained from experimental data. Recently, Goodwin et al.³⁰ used reverse Monte Carlo modeling of synchrotron X-ray scattering data to generate atom positions for hydrous ACC ($\text{H}_2\text{O}/\text{CaCO}_3 = 1.0$).³⁰ Their ACC model consists of a nanoporous structure with Ca-rich volumes and a network of water and carbonate-rich channels. The Ca-rich volumes contain short-range structural features that resemble those of the crystalline calcium carbonate phases, although the model contains some interatomic distances that are probably too short.³¹ Our previous molecular dynamics (MD) simulation starting with the atom positions in one of their models shows

Received: August 22, 2012

Revised: February 26, 2013

Published: February 26, 2013

substantial structural rearrangement resulting in increased computed density and shrinkage of the water-rich channels.³¹

There have been several recent computational studies of the formation of ACC from aqueous solution, the nature of prenucleation clusters (PNCs),^{32–34} the structural characteristics of bulk ACC,^{31,35–38} and the mechanism of its formation.³⁸ Ab initio calculations for small hydrated clusters of calcium (bi)carbonate³⁹ provide information about the binding affinities and stable local geometries. Ab initio molecular dynamics (AIMD) simulations have provided understanding of the formation of calcium (bi)carbonate ion pairs in bulk water⁴⁰ and the structure of first hydration shell around the solvated ions.^{40,41} Free-energy calculations from classical MD simulations of PNCs indicate that the energy penalty to add a Ca^{2+} , CO_3^{2-} ion pair to a cluster is negligible, implying favorable energetics for formation of the amorphous phase from solution.³⁵ This process is found to be exothermic with increasing cluster size up to a critical diameter of ~ 4 nm.

Here, we present the results of a computational molecular dynamics (MD) study of the dehydration of ACC that provide new insight into the structural and energetic changes that occur with dehydration. These calculations are based on our computed structure³¹ that was obtained by MD simulation beginning with the reverse Monte Carlo structure of Goodwin et al.³⁰ The results here show that dehydration causes substantial local and intermediate range structural rearrangement that leads to an increase in density. The model with no water has a density essentially equal to that of calcite. This dehydration is endothermic, and the dehydration energy increases with decreasing water content. This change is correlated with an increasingly strong hydrogen bond (H-bond) network in less hydrated ACC. Analysis of the near neighbor arrangements of Ca^{2+} and H_2O molecules around the CO_3^{2-} groups show that they occupy well-defined regions around the CO_3^{2-} ions.

SIMULATION DETAILS

Classical molecular dynamics (MD) simulations were performed for ACC with $\text{H}_2\text{O}/\text{CaCO}_3$ ratios of 1.0, 0.9, 0.67, 0.5, 0.25, and 0.0 (anhydrous). These ACC systems are referred to as S1.0 (1.0 mol), S0.9 (0.9 mol), S0.67 (0.67 mol), S0.5 (0.5 mol), S0.25 (0.25 mol), and Sd (anhydrous). The initial atomic configuration was the final configuration from the simulation of Singer et al.³¹ for the sample with $\text{H}_2\text{O}/\text{CaCO}_3 = 1.0$. Model systems were built by progressively removing the appropriate number of randomly chosen water molecules to yield desired $\text{H}_2\text{O}/\text{CaCO}_3$ ratios. Each simulated system contains 1620 formula units of CaCO_3 (N_{CaCO_3}) and the required number of water molecules ($N_{\text{H}_2\text{O}}$).

To validate the influence from the initial configuration based on the Singer et al.³¹ structural model, we performed a second set of simulations of ACC with a $\text{H}_2\text{O}/\text{CaCO}_3$ ratio of 1.0 beginning from a different initial configuration (R1.0) and with the same computational method (see Supporting Information). This system was modeled with a geometry optimized $\text{CaCO}_3 \cdot 1\text{H}_2\text{O}$ cluster repeated 1620 times in an orthorhombic box. After 2 ns of isothermal–isobaric (NPT) simulation, the structural features of this system were essentially identical to those of system S1.0. This result is consistent with previous computational work showing that the rate of exchange of water molecules in the nearest neighbor coordination shell of Ca^{2+} is quite fast on the MD time scale.⁴² All the results presented

hereafter are from the first set of simulations starting from the S1.0 model.

All MD simulations were run using the DL_POLY4.0⁴³ software package with three-dimensional periodic boundary conditions. We used the flexible force field parameters of Raiteri and Gale,³⁵ which allow out-of-plane bending of the CO_3^{2-} groups. The nonbonded interactions were truncated at 9 Å. The Nosé–Hoover chain thermostat and barostat⁴⁴ were employed to control the system temperature and pressure with a 0.1 ps relaxation time. The Ewald⁴⁵ formalism was used to evaluate electrostatic interactions. To generate S0.9, water molecules were removed randomly from S1.0 and 4 ns of NPT simulation was performed to attain the equilibrium density of the system at 300 K and 1 atm pressure followed by 3 ns of isothermal–isochoric (NVT) simulation. The results presented here are from the last 2 ns of the NVT simulation trajectory. Subsequently, S0.67 was generated from the equilibrated S0.9 structure using the same procedure. These steps were repeated for S0.5, S0.25 and Sd. Table 1 lists the system compositions,

Table 1. System Specifications of ACC at Different Hydration Level

system	$\text{H}_2\text{O}/\text{CaCO}_3$ (mol)	density (gm/ cc)	orthorhombic box dimensions (Å ³)
S1.0	1.00	2.59	52.0 × 54.0 × 44.0
S0.9	0.90	2.63	51.1 × 53.0 × 43.7
S0.67	0.67	2.67	50.2 × 52.1 × 43.0
S0.5	0.50	2.69	49.6 × 51.5 × 42.4
S0.25	0.25	2.70	49.0 × 50.7 × 41.9
Sd	0.00	2.71	48.1 × 50.0 × 41.2

simulation cell dimensions, and computed densities. In the nomenclature of this paper, O_W is the oxygen of a water and O_C is the oxygen of a carbonate ion.

The radial distribution functions (RDFs) of ACC and relevant crystalline phases were calculated with a resolution of 0.05 Å. The RDFs obtained for the crystalline structures were convoluted with a Gaussian function of width 0.05 Å to mimic thermal broadening. The density isosurfaces provide three-dimensional information about the local coordination environments. The probability densities are calculated by averaging over the last 2 ns of NVT simulations with an ensemble average over identical chemical species.⁴⁶ For these calculations, the volume of each grid was chosen to be 0.008 Å³.

For hydrogen bond analyses, we define a H-bond if three geometric criteria between the acceptor (A) and donor (D) species are met simultaneously.⁴⁷ Let O_A and O_D denote the acceptor and donor oxygens, respectively, and H_D be the donor hydrogen. For a H-bond, the nearest neighbor $\text{H}_\text{D}-\text{O}_\text{A}$ and $\text{O}_\text{A}-\text{O}_\text{D}$ distances are the distances of the first minima of the radial distribution functions. These values are 2.5 and 3.5 Å, respectively. Because the H-bond interaction is directional and has a nearly linear geometry for the angle $\text{O}_\text{A}-\text{H}_\text{D}-\text{O}_\text{D}$, this angle is expected to be between 140° and 180°. In our systems, H-bond donors are always water molecules, and we distinguish those in which the acceptor is the oxygen of a carbonate anion or another water molecule.

RESULTS AND DISCUSSION

System Density. With progressive dehydration, the computed equilibrium densities (ρ) of ACC increase and the orthorhombic cell dimensions decrease (Figure 1, Table 1).

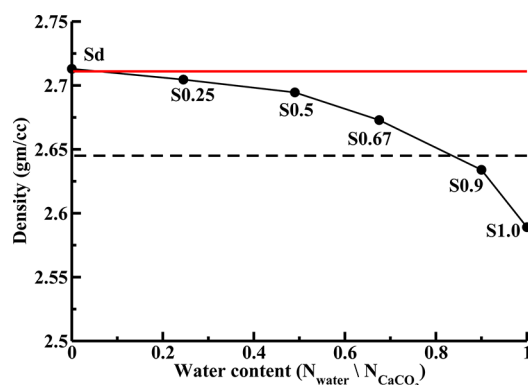


Figure 1. ACC densities at varying hydration level. The density of calcite is shown by the red line and that of vaterite by the dashed black line. The density of sample S1.0 is taken from ref 31.

The density of ACC with $\text{H}_2\text{O}/\text{CaCO}_3 = 1.0$ is 2.59 g/cm^3 , about 7% higher than that of monohydrocalcite (2.42 g/cm^3). For the fully anhydrous ACC (Sd), the computed density is 2.71 g/cm^3 , essentially equal to the value for calcite⁴⁹ ($\rho = 2.75 \text{ g/cm}^3$) but greater than that of vaterite⁵⁰ (2.65 g/cm^3), and substantially less than that of aragonite⁵¹ (2.95 g/cm^3). There are few published ACC densities with which to compare these values. In a time-resolved small-angle X-ray scattering (SAXS) study of ACC crystallization, Bolze et al.⁵² showed that an ACC with a density of 1.62 g/cm^3 transforms to calcite through dissolution and crystallization.⁵³ The initial water content of the ACC sample in that study was equivalent to a composition of $\text{CaCO}_3 \cdot 6\text{H}_2\text{O}$, and its density was determined by evaluation of the absolute SAXS scattering intensities. Unfortunately, there are no published, experimentally determined densities for ACCs with $\text{H}_2\text{O}/\text{CaCO}_3$ ratios between 0.0 and 1.0, the values studied here.

The similarity in the compositions and densities of monohydrocalcite and ACC phases suggests that the monohydrocalcite structure may be a good model for that of biogenic and synthetic hydrous ACC, as previously suggested by Levi and co-workers.^{24,25} However, EXAFS studies of ACCs obtained from different sources show that the local structural environment of Ca^{2+} varies significantly among the different samples, suggesting that neither the monohydrocalcite structure nor that of any other crystalline phase is likely to be a good model for all ACC samples.^{21,54,55}

Structural Changes Due to Dehydration. Origin of the Density Increase and Partial Radial Distribution Functions. The structural origin of the increasing ACC density with decreasing water content involves changes in both the nearest neighbor (NN) coordination and correlations at longer distances. At the nearest neighbor scale, the average coordination of Ca^{2+} by O_W (n_{O_W}) decreases and its coordination by O_C (n_{O_C}) increases, resulting in a net decrease in NN O-atoms (n_{total}) from 7.8 to 7.0 (Figure 2a). In parallel, the number of NN CO_3^{2-} groups (n_C , first neighbor Ca–C coordination) increases from 5.0 to 6.0 due to O_C replacing O_W in the NN shell. In monohydrocalcite, Ca^{2+} is coordinated by a total of 8 oxygen atoms within a cutoff distance of 2.82 \AA , and the nearest neighbor Ca–C coordination is 4 at a cutoff distance of 4.0 \AA . Thus, ACC with a $\text{H}_2\text{O}/\text{CaCO}_3$ ratio of 1.0 (S1.0) has an overall lower Ca–O coordination and higher Ca–C coordination than monohydrocalcite, contributing to its higher density. The crystalline calcium carbonate phases show a

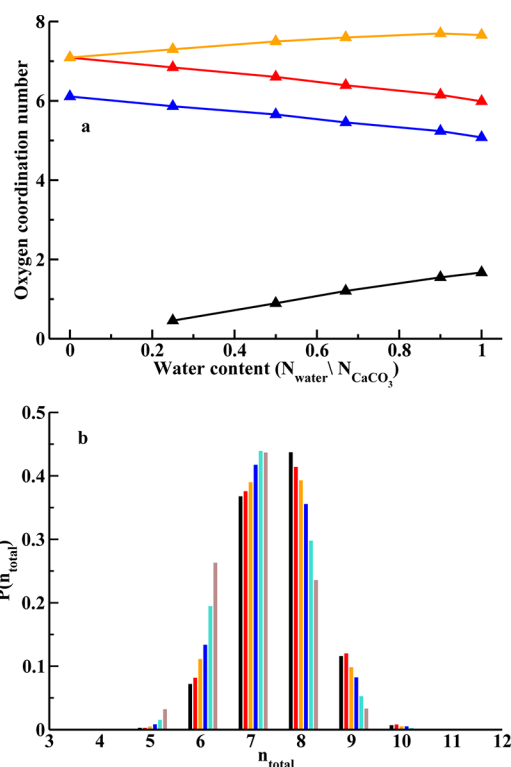


Figure 2. (a) Average coordination number of oxygen and carbon within the first coordination shell of Ca^{2+} . The cutoff distances for defining coordination are the positions of first minima in the respective partial RDFs (Figure 3). Color coding: n_{O_W} (black), n_{O_C} (red), n_{total} (orange), n_C (blue); (b) Distribution of total oxygen coordination number within 2.8 \AA of a Ca^{2+} ion in S1.0 (black), S0.9 (red), S0.67 (orange), S0.5 (blue), S0.25 (turquoise), Sd (gray).

similar trend of decreasing Ca–O coordination with decreasing water content. The values of n_{O_C} , n_{O_W} , and n_{total} are 6, 2, and 8 for ikaite, whereas these are 7, 1, and 8 in monohydrocalcite, respectively. In both calcite and vaterite, Ca^{2+} is coordinated by 6 O_C atoms within a cutoff distance of 2.8 \AA . The n_{O_C} is 9 in aragonite, the dense and high pressure phase of calcium carbonate. As expected for a disordered material, the Ca–O coordination in the simulated ACCs is heterogeneous with values between 5 and 10 (Figure 2b). The most probable value of n_{total} decreases from 8 for S1.0 to 7 for Sd.

Closer packing of the CO_3^{2-} groups also plays an important role in the density changes. The C–C radial distribution function ($g_{\text{C}-\text{C}}(r)$; Figure 3a) contain two peaks at $r_{\text{C}-\text{C}} = 4.7 \text{ \AA}$ and $r_{\text{C}-\text{C}} = 6.0 \text{ \AA}$, and the intensity of a small hump at 4 \AA for S1.0 increases with dehydration and gradually becomes a distinct peak at 3.5 \AA for Sd. From S1.0 to Sd, the running coordination number ($N_{\text{C}-\text{C}}$) increases from 1.7 to 2.7 at 4 \AA , from 9.0 to 11.5 at 5.5 \AA , and 18.3 to 22.8 at 7.0 \AA . At longer distances, $N_{\text{C}-\text{C}}$ at 8 \AA increases from 26.6 for S1.0 to 33.3 for Sd.

Increased second neighbor Ca–Ca packing is also a major contributor to the increase in density, as shown in the Ca–Ca radial distribution function ($g_{\text{Ca}-\text{Ca}}(r)$; Figure 3b). The Ca–Ca coordination number ($N_{\text{Ca}-\text{Ca}}$) within the first minima (at $r_{\text{Ca}-\text{Ca}} = 5.0 \text{ \AA}$) increases from 6.3 for S1.0 to 8.6 for Sd and within the second minima at $r_{\text{Ca}-\text{Ca}} = 7 \text{ \AA}$, $N_{\text{Ca}-\text{Ca}}$ increases from 18.3 for S1.0 to 22.5 for Sd.

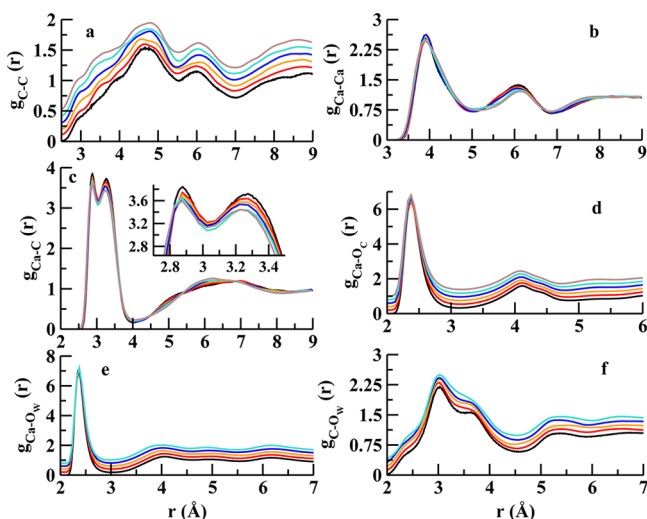


Figure 3. Intermolecular radial distribution functions for (a) C–C, (b) Ca–Ca, (c) Ca–C, (d) Ca–O_C, (e) Ca–O_W, and (f) C–O_W in S1.0 (black), S0.9 (red), S0.67 (orange), S0.5 (blue), S0.25 (turquoise), and Sd (gray). The first peak of $g_{\text{Ca-C}}(r)$ is expanded in the inset of panel c. The partial RDFs in panels a, d, e, and f are shifted along the Y-axis for better viewing.

Despite the density increase from S1.0 to Sd, the main features in the radial distribution functions (RDFs) are present at all hydration levels (Figure 3). The Ca–C RDFs ($g_{\text{Ca-C}}(r)$; Figure 3c) contain two maxima, one at ~ 2.7 Å and the other at 3.2 Å, representing different Ca²⁺ coordinations with the carbonate groups. Both maxima show a small but systematic reduction in intensity with dehydration. The running coordination number of C atoms within the first minima at ~ 4 Å are 5.1 for S1.0 and 6.1 for Sd. For S1.0, there is a broad peak for the second coordination shell with a hump at ~ 5 Å and a maxima at ~ 7 Å. During dehydration, the intensity of the hump at 5 Å gradually decreases, and the peak maximum moves to ~ 6 Å resulting in a more distinct second coordination shell in Sd.

The RDFs between Ca²⁺ and the oxygens of the CO₃²⁻ groups ($g_{\text{Ca-O}_C}(r)$; Figure 3d) and water ($g_{\text{Ca-O}_W}(r)$; Figure 3e) show that the nearest neighbor interatomic distances do not change significantly but the coordination numbers do. In contrast, there are marked changes in the distribution of water oxygens around CO₃²⁻ as evident from the $g_{\text{C-O}_W}(r)$ in Figure 3f. For S1.0, $g_{\text{C-O}_W}(r)$ shows two distinct peaks at 3.0, and 3.6 Å implying two different structural arrangement of O_W around carbonate ions. The intensity of the second peak at 3.6 Å decreases with dehydration and becomes a hump in the least hydrated ACC (S0.25).

Total Radial Distribution Functions. The total RDFs ($g_{\text{total}}(r)$) for hydrous (S1.0 and S0.5) and anhydrous (Sd) ACC (Figure 4, 5) show well resolved maxima at 1.1 (for hydrous ACC), 1.28, 1.75 (for hydrous ACC), 2.25, 3.0, 4.0, 5.1, and 6.3 Å. Correlations at longer distances are not resolvable. The first two peaks represent the intramolecular bond lengths in water and carbonate groups, respectively. These bond lengths were constrained to these values by the force field parameters. The intra- and intermolecular correlations correspond well with the experimental pair distribution functions of ACC obtained from X-ray scattering data.¹⁰ The intensities of the experimental data are weighted by the scattering factors of the individual

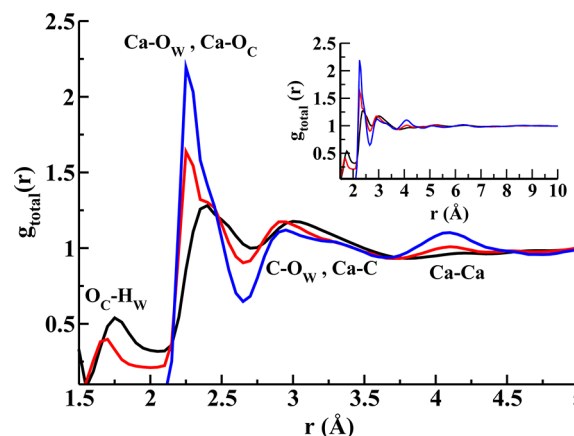


Figure 4. Total radial distribution functions for S1.0 (black), S0.5 (red), and Sd (blue). Intramolecular correlations are not included. The major atomic correlations contributing to each peak are shown. The inset shows the same plots up to 10 Å.

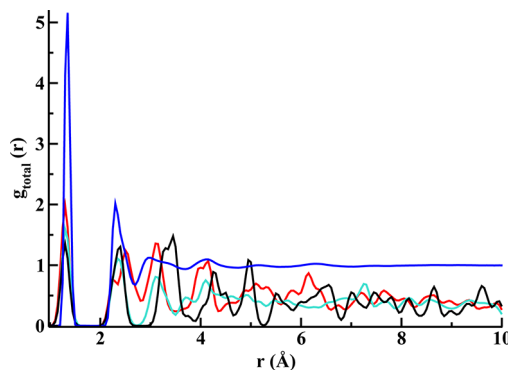


Figure 5. Total radial distribution functions of anhydrous ACC (blue), calcite (black), aragonite (red), and vaterite (turquoise). The RDFs obtained for the crystalline structures are convoluted with a Gaussian function of width 0.05 Å to mimic the broadening due to thermal vibrations.

elements, whereas the computed RDFs are not. As discussed in previous studies,^{21,31} the lack of long-range interatomic correlations is expected for an amorphous material. The similarity of the experimental and computed correlations for the hydrous phases supports the usefulness of the computed results in understanding the dehydration.

Comparison of $g_{\text{total}}(r)$ with the partial intermolecular pair-correlation functions (not shown) shows that the maximum at 1.75 Å corresponds to the hydrogen bond interaction between O_C and O_W. This peak is absent for the anhydrous ACC. The peaks and shoulders between 2.25 and 2.5 Å are due predominantly to correlations of Ca²⁺ with O_W and O_C. For S1.0, this peak at 2.4 Å and a shoulder at 2.5 Å narrow and shift to smaller values with decreasing hydration, and there are two resolvable components for Sd. At the respective minima following these peaks, the coordination numbers are 68, 64.6, and 62.0 for systems S1.0, S0.5, and Sd, respectively.

The peak at ~ 3.0 Å is due to the NN Ca–C and C–O_W correlations, and for the anhydrous system entirely to Ca–C. The total coordination numbers (including the bonded atoms) at the third minima are 224 at 3.8 Å and 190 at 3.65 Å in S1.0 and Sd, respectively. At longer distances, a Ca–Ca correlation appears at 4.1 Å in S0.5 and grows in intensity with progressive dehydration. As discussed above, this increase in peak intensity

is associated with a denser and more ordered second coordination shell in the less hydrated and anhydrous ACC. In addition to these prominent peaks, there are two low-intensity peaks at ~ 5.1 and ~ 6.3 Å that are not dominated by specific pair correlations.

Comparison with the Anhydrous Crystalline Phases of Calcium Carbonate. Comparison of the RDFs of anhydrous ACC (Sd) and those of the anhydrous crystalline phases of calcium carbonate (calcite,⁴⁹ vaterite,⁵⁰ and aragonite;⁵¹ Figure 5) shows that similar interatomic correlations are present within 6.3 Å at broadly similar distances for all the phases, but that the correlations in ACC are not similar in detail to those of any of the crystalline phases. The RDFs for the crystalline phases were obtained from the experimental crystal structures. To mimic vibrational broadening, the RDFs of the crystalline phases were convoluted with a Gaussian function of width 0.05 Å.

For all systems, the first peak at 1.28 Å is the intramolecular C–O_C distance in carbonate groups. The prominent peaks for Sd at 2.3, 2.9, and 4.12 Å corresponding to the peaks for calcite at 2.4, 3.45, and 4.28 Å, for vaterite at 2.36, 3.1, and 4.1 Å, and for aragonite at 2.52, 3.14, and 4.17 Å. These peaks are assigned to specific pair interactions based on comparison with the partial RDFs and the X-ray absorption spectroscopic (XAS) data for calcite.¹⁰

Within 2.69 Å, which can be thought of as the first neighbor coordination shell, the RDF for Sd resembles those of calcite and vaterite more than aragonite, as expected for the larger Ca–O_C coordination of aragonite compared to ACC, calcite, and vaterite. The second and third peaks at 2.3 and 4.1 Å for ACC are broad and cover the corresponding maxima of all three crystalline phases, which are slightly different from each other. At longer distances, the peaks at 5.1 and 6.3 Å for Sd are at distances present for aragonite and calcite but not for vaterite.

Near-Neighbor Structure around CO₃²⁻. The presence of two maxima in the $g_{\text{Ca-C}}(r)$ s of the ACCs between 2.8 and 4.0 Å is due to a quite ordered angular distribution of Ca²⁺ ions around the CO₃²⁻ groups and shows that the short-range distribution of Ca²⁺ ions in anhydrous ACC (Sd) is more similar to that of calcite than to the other crystalline phases (Figure 6). This angular relationship can be described by the angle, θ , between the normal to the plane of CO₃²⁻ anion and the vector between C (carbon) and the neighboring Ca²⁺ ions that are located within 4.0 Å of the C. The distributions of θ for all the ACCs have maxima at $\theta = 60^\circ$ and 120° and minima at 90° , showing that the Ca²⁺ ions prefer a nonplanar geometry in which Ca²⁺ ions are located 30° above and below the carbonate plane. The intensity of this distribution at 90° decreases with decreasing water content, showing increasing preference for the 30° out-of-plane geometry at low water contents.

Earlier computational studies have indicated that the most favorable geometry of the Ca²⁺ and CO₃²⁻ complex in the gas phase is bidentate⁵⁶ with Ca²⁺ coplanar with CO₃²⁻ ($\theta = 90^\circ$) and equidistant to two oxygen atoms of the CO₃²⁻ ion. A similar coplanar geometry occurs in the crystalline calcium carbonate hexahydrate phase, ikaite (CaCO₃·6H₂O), for which $P(\theta)$ has a single peak centered at $\theta = 90^\circ$ (Figure 6). In vaterite, two of the Ca²⁺ ions are coplanar and four are out-of-plane within 4 Å of CO₃²⁻ (Figure 7). For monohydrocalcite, there is a broad distribution between 50° and 90° , and for aragonite there are two intense peaks at 75° and 125° and two low intensity peaks at 60° and 110° . For calcite, all six Ca²⁺

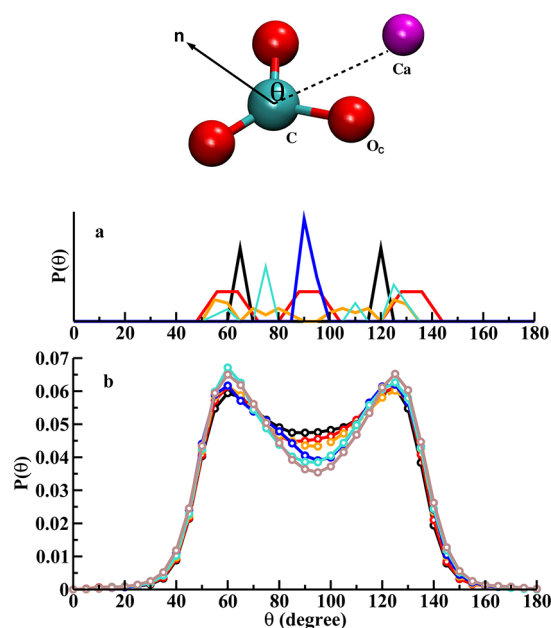


Figure 6. (Upper panel) Schematic representation of the angle θ . The normal to the carbonate plane is denoted by vector \hat{n} . (Lower panel) (a) Distribution of angle θ for the crystalline phases of calcium carbonate, calcite (black), vaterite (red), aragonite (turquoise), monohydrocalcite (orange), and ikaite (blue). (b) Distribution of θ in S1.0 (black), S0.9 (red), S0.67 (orange), S0.5 (blue), S0.25 (turquoise), and Sd (gray).

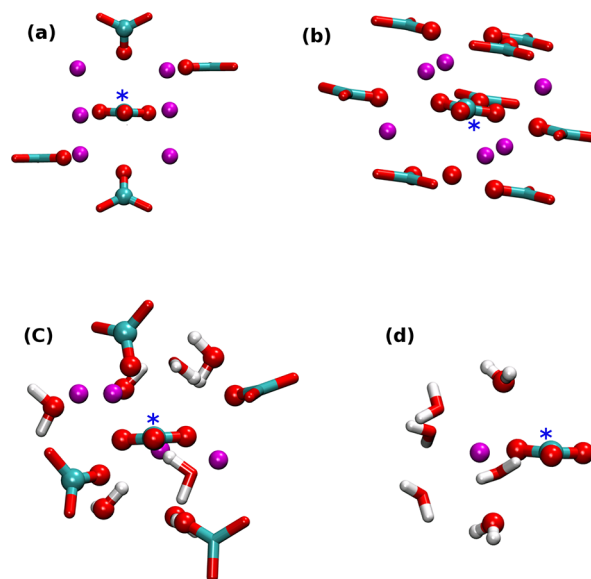


Figure 7. Arrangement of atoms (ball-and-stick representation) within 4 Å of a central CO₃²⁻ group (marked with asterisk) in (a) vaterite, (b) calcite, (c) monohydrocalcite, (d) ikaite. Color code: oxygen (red), carbon (turquoise), hydrogen (white), calcium (magenta).

near-neighbors (Figure 7) within 4.0 Å from C_{CO₃} are at $\theta = 60^\circ$ and $\theta = 120^\circ$ (Figure 6).

The atomic density isosurfaces of Ca²⁺ and O_w (Figure 8) around carbonate groups confirm that the near-neighbor Ca²⁺ ions are preferentially located within 30° from the carbonate plane and provide a more detailed, 3-dimensional picture of the local structure. In the hydrated system S0.9, the Ca²⁺ ions in the first peak of the Ca–C RDF ($r < 2.9$ Å) are distributed in an

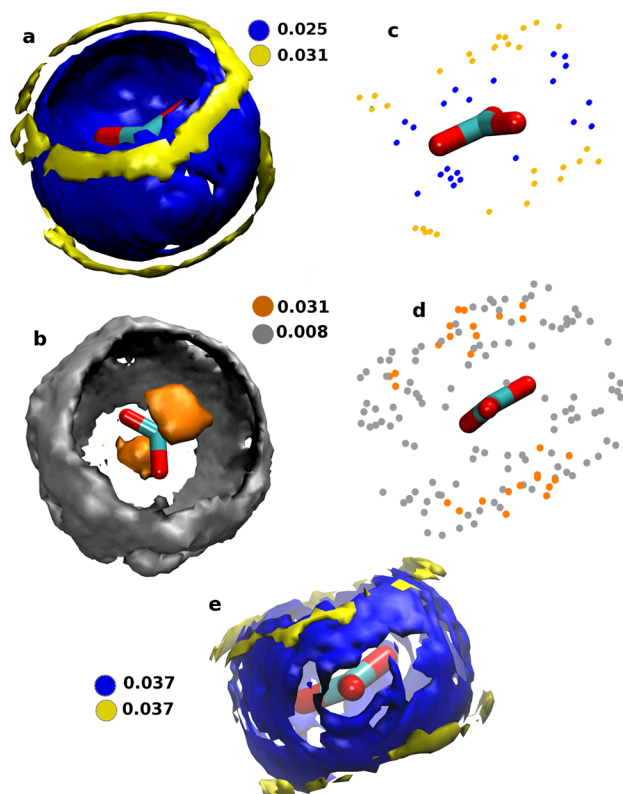


Figure 8. Density isosurfaces of Ca²⁺ ions (a, c, e) and oxygen atoms of water (O_W) (b, d) in the first coordination shell of CO₃²⁻ in (a, b) S0.9, (c, d) monohydrocalcite, and (e) Sd. Isosurfaces (a, c, e) for two distance ($r_{\text{C}-\text{Ca}}$) cut-offs between Ca²⁺ and C, (i) 2.9 Å > $r_{\text{C}-\text{Ca}}$ (blue) and (ii) 3.75 Å > $r_{\text{C}-\text{Ca}}$ > 3.15 Å (yellow), are shown here. The distance ($r_{\text{C}-\text{O}_\text{W}}$) cut-offs in parts b and d between C and O_W are (i) 3.3 Å > $r_{\text{C}-\text{O}_\text{W}}$ (orange) and (ii) 4.4 Å > $r_{\text{C}-\text{O}_\text{W}}$ > 3.4 Å (gray). The data are ensemble averaged over all the molecules in the system, and across the entire MD trajectory. The color codes are in units of atoms per Å³.

annulus between -30° and $+30^\circ$ to the plane of the carbonate groups. There appears to be no preference for monodentate or bidentate coordination. In the second Ca–C NN RDF peak between 3.15 and 3.75 Å, the calcium ions are distributed on annuli at 30° below and above the carbonate plane. Again, there is no preference for monodentate or bidentate coordination. These distributions are quite similar to those in monohydrocalcite with the same cut off distances (Figure 8c).

For system S0.9, the O_W isoprobability surfaces are the complement of the Ca²⁺ surfaces (Figure 8b). Within the first coordination shell of $g_{\text{C}-\text{O}_\text{W}}(r)$ at $r_{\text{C}-\text{O}_\text{W}} < 3.3$ Å, almost all the water molecules are highly localized, perpendicular to the CO₃²⁻ plane. At longer distances, 3.4 Å < $r_{\text{C}-\text{O}_\text{W}} < 4.4$ Å, water molecules are mostly arranged in an annulus between 30° to the plane of CO₃²⁻ forming a stable hydrophilic region through strong H-bond interactions with the central carbonate group. In contrast, the water molecules in the polar regions are less likely to make H-bonds with the central carbonate group due to the geometric constraints and thus can be called loosely bound. During dehydration, the atomic densities in these regions decrease, facilitating the reduction in the distances between neighboring carbonate groups and leading to increased parallel orientation of the CO₃²⁻ groups as in calcite.

As for the C–Ca distributions, the C–O_W distribution is broadly similar to that in monohydrocalcite, with the nearest

O_W atoms located above and below the carbonate plane and the ones further away located in rings above and below the plane of the carbonate. In anhydrous ACC (Sd), the distribution of Ca²⁺ around the CO₃²⁻ groups is more ordered (Figure 8e), consistent with the decreased probability at 90° shown in Figure 6. In this distribution, Ca²⁺ ions in the first subpeak of $g_{\text{Ca}-\text{C}}(r)$ ($r_{\text{Ca}-\text{C}} < 2.9$ Å) occur principally in an annulus within 30° of the carbonate plane, as in system S0.9. They are, however, less likely to occur along the extension of the C–O_C bond vector resulting in voids in the isoprobability surface and showing a strong preference of these atoms for bidentate coordination.

Energetics of ACC Dehydration. The computed dehydration enthalpies for ACC show increasingly negative values with decreasing water content (Figure 9). This result suggests

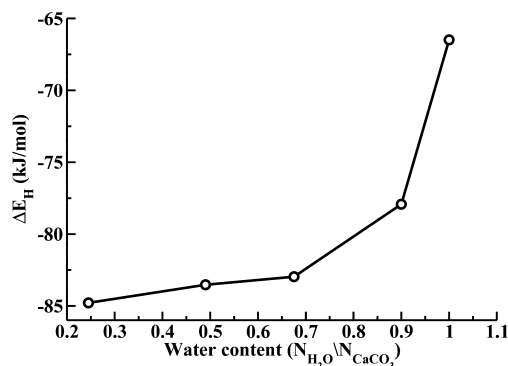


Figure 9. Enthalpy of hydration per water molecule (ΔE_{H}) with respect to anhydrous ACC.

that increasingly favorable H-bond interactions with decreasing water content make the system energetically more stable. The experimentally observed enthalpy for complete dehydration of an ACC with a H₂O/CaCO₃ ratio of 1.6 is ~ 40 kJ/mol, which is similar to the heat of vaporization of bulk water.^{20,57} In the present work, the H₂O/CaCO₃ ratio is 1.0 in the most hydrated ACC (S1.0). This water content is much less than in the experimental sample, and thus a direct comparison of the enthalpy values is not possible.

We evaluated the energetics of ACC dehydration using the dehydration enthalpy, which is the calculated difference in system enthalpy between hydrated and anhydrous ACC (Figure 9). The dehydration enthalpy per water molecule (ΔE_{H}) is defined as^{58,59}

$$\Delta E_{\text{H}} = \frac{\langle E(N_{\text{H}_2\text{O}}) \rangle - \langle E(0) \rangle}{N_{\text{H}_2\text{O}}} \quad (1)$$

where $N_{\text{H}_2\text{O}}$ is the number of water molecules present in the hydrated amorphous phase, $\langle E(N_{\text{H}_2\text{O}}) \rangle$ is the average enthalpy of the hydrated system, and $\langle E(0) \rangle$ is the average enthalpy of the dehydrated system. The increasingly negative ΔE_{H} values with decreasing water content is due to the progressively more ordered local structure with decreasing water content. The increasing order is illustrated, for instance, by the more ordered distribution of Ca²⁺ ions in the first coordination shell of CO₃²⁻ (Figure 6, Figure 8). Bots et al.⁵⁷ drew the same conclusion based on the X-ray diffraction patterns of hydrous ACC. These patterns become increasingly better resolved with decreasing water content.

In our model ACC systems, there are substantial changes in the fraction of H-bonds accepted by O_C (F_{CO_3}) and O_W (F_{wat} ; Figure 10) with decreasing water content, also contributing to

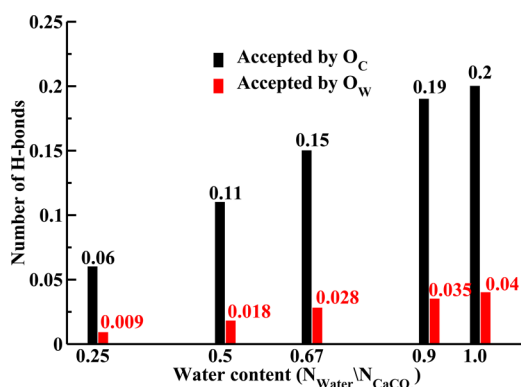


Figure 10. Number of H-bonds accepted by O_C of CO_3^{2-} (black) and O_W of water molecule (red).

the increasing dehydration enthalpy. In the most hydrated ACC (S1.0), the fraction of H-bonds accepted by O_C and O_W are 0.2 and 0.04, respectively. The large difference between these values is due to the larger strength of the H-bonds accepted by O_C , as shown in a previous ab initio molecular dynamics study of solvated carbonate species in bulk water.⁶⁰ These ab initio calculations show that strong $O_C \cdots H_W - O_W$ H-bond interaction results in shorter H-bond lengths and longer H-bond life times compared to $O_W \cdots H_W - O_W$ H-bonds. Both F_{CO_3} and F_{wat} decrease with decreasing water content, and the fraction $F_{CO_3}/(F_{CO_3} + F_{wat})$ of $O_C \cdots H_W - O_W$ H-bonds increases gradually from 0.83 in S1.0 to 0.87 in S0.25 indicating more favorable interaction between these species in less hydrated ACC. Also, the fraction of free water molecules, those that neither donate nor receive a H-bond, decreases from 0.52 in S1.0 to 0.46 in S0.25.

CONCLUSIONS

Computational molecular dynamics modeling of hydrated and anhydrous ACC provides detailed, molecular scale understanding of the evolution of the local structural environment in this important transient phase in calcium carbonate crystallization as water content decreases. Starting from a hydrated ACC system with a $H_2O/CaCO_3$ ratio of 1.0, the density increases from 2.59 to 2.71 g/cm³ for anhydrous ACC. The density of the anhydrous ACC is essentially equal to that of calcite. This increase in density is due to increasing local ordering resulting in denser packing of near neighbor atoms, with significant changes visible at distances up to ~ 4.5 Å. Water loss leads to increasing coordination of Ca^{2+} by the oxygens of carbonate groups. In contrast, within the first coordination shell of Ca^{2+} , the number of coordinating oxygen atoms of water molecules decreases resulting in a decrease in the total near neighbor coordination number. This trend is similar to that for crystalline phases of calcium carbonate with decreasing water content and increasing density; ikaite ($CaCO_3 \cdot 6H_2O$) \rightarrow monohydrocalcite ($CaCO_3 \cdot H_2O$) \rightarrow calcite/vaterite.

The increasing ordering caused by dehydration is reflected in the near neighbor coordination relationships among Ca^{2+} , CO_3^{2-} , and H_2O . In hydrated ACC, Ca^{2+} and H_2O occupy specific locations around the carbonate anions. The nearest

Ca^{2+} ions are distributed mostly within an annulus that spans between $\sim 30^\circ$ below and above the plane of the carbonate group. In contrast, the nearest water oxygens (within 3.0 Å from carbon) preferentially occupy the polar regions perpendicular to the carbonate plane. For hydrated ACC, the nearest neighbor interaction between Ca^{2+} and CO_3^{2-} shows no preference for either bidentate or monodentate coordination. In dehydrated ACC, the in-plane monodentate geometry is less probable and leads to voids in the isoprobability surface of calcium along the extension of the C– O_C bond. Water molecules located between 3.4 and 4.4 Å of the central carbon atom are located in an annulus between -30° and $+30^\circ$ of the plane of the carbonate group and form strong H-bonds with the carbonate groups. Ca^{2+} ions within 3.15 and 3.75 Å from the central carbon atom are located in two rings at $+30^\circ$ and -30° from the plane of the CO_3^{2-} groups. The fraction of H-bonds donated by water molecules to CO_3^{2-} increases with dehydration, and the fraction of non-H-bonded water molecules decreases. The increasingly strong H-bond interactions between CO_3^{2-} and water along with the more ordered local structure lead to an increasing hydration energy with decreasing water content.

The results presented here provide insight into the microscopic details of the complicated ACC structure that cannot be obtained experimentally. We will undertake similar studies of ACC containing a variety of impurities to elucidate their roles in stabilizing the ACC phases.

ASSOCIATED CONTENT

Supporting Information

Details of the modeling of a second hydrous ACC sample with a $H_2O/CaCO_3$ ratio of 1.0 that we started from an ordered initial configuration. The structure in this model is essentially identical to that described in the full paper. This material is available free of charge via the Internet at <http://pubs.acs.org/>.

AUTHOR INFORMATION

Corresponding Author

*E-mail: saharaym@msu.edu. Tel.: +1 (517) 355-9715 ext 336. Fax: +1 (517) 432-1054.

Notes

The authors declare no competing financial interest.

ACKNOWLEDGMENTS

This work was supported by the United States Department of Energy, Office of Basic Energy Science through Grants DEFG02-10ER16128 and DE-FG02-08ER15929. We thank Prof. Geoffrey Bowers and Mr. Jared Singer for helpful discussions about ACC.

REFERENCES

- (1) Meldrum, F. Calcium Carbonate in Biomineralisation and Biomimetic Chemistry. *Int. Mater. Rev.* **2003**, *48*, 187–224.
- (2) Xu, G.; Yao, N.; Aksay, I.; Groves, J. Biomimetic Synthesis of Macroscopic-Scale Calcium Carbonate Thin Films. Evidence for a Multistep Assembly Process. *J. Am. Chem. Soc.* **1998**, *120*, 11977–11985.
- (3) Benson, S.; Cole, D. CO_2 Sequestration in Deep Sedimentary Formations. *Elements* **2008**, *4*, 325–331.
- (4) Doughty, C. Investigation of CO_2 Plume Behavior for a Large-Scale Pilot Test of Geologic Carbon Storage in a Saline Formation. *Transport Poros Med.* **2010**, *82*, 49–76.

- (5) Ketzer, J.; Iglesias, R.; Einloft, S.; Dullius, J.; Ligabue, R.; De Lima, V. Water–Rock–CO₂ Interactions in Saline Aquifers Aimed for Carbon Dioxide Storage: Experimental and Numerical Modeling Studies of the Rio Bonito Formation (Permian), Southern Brazil. *Appl. Geochem.* **2009**, *24*, 760–767.
- (6) Addadi, L.; Raz, S.; Weiner, S. Taking Advantage of Disorder: Amorphous Calcium Carbonate and Its Roles in Biomineralization. *Adv. Mater.* **2003**, *15*, 959–970.
- (7) Weiner, S.; Levi-Kalishman, Y.; Raz, S.; Addadi, L. Biologically Formed Amorphous Calcium Carbonate. *Connect. Tissue Res.* **2003**, *44*, 214–218.
- (8) Weiss, I.; Tuross, N.; Addadi, L.; Weiner, S. Mollusc Larval Shell Formation: Amorphous Calcium Carbonate Is a Precursor Phase for Aragonite. *J. Exp. Zool.* **2002**, *293*, 478–491.
- (9) Beniash, E.; Aizenberg, J.; Addadi, L.; Weiner, S. Amorphous Calcium Carbonate Transforms into Calcite During Sea Urchin Larval Spicule Growth. *Proc. R. Soc., B-Biol. Sci.* **1997**, *264*, 461–465.
- (10) Politi, Y.; Levi-Kalishman, Y.; Raz, S.; Wilt, F.; Addadi, L.; Weiner, S.; Sagi, I. Structural Characterization of the Transient Amorphous Calcium Carbonate Precursor Phase in Sea Urchin Embryos. *Adv. Funct. Mater.* **2006**, *16*, 1289–1298.
- (11) Politi, Y.; Metzler, R.; Abrecht, M.; Gilbert, B.; Wilt, F.; Sagi, I.; Addadi, L.; Weiner, S.; Gilbert, P. Transformation Mechanism of Amorphous Calcium Carbonate into Calcite in the Sea Urchin Larval Spicule. *Proc. Natl. Acad. Sci. U.S.A.* **2008**, *105*, 17362.
- (12) Aizenberg, J.; Lambert, G.; Weiner, S.; Addadi, L. Factors Involved in the Formation of Amorphous and Crystalline Calcium Carbonate: A Study of an Ascidian Skeleton. *J. Am. Chem. Soc.* **2002**, *124*, 32–39.
- (13) Aizenberg, J.; Ilan, M.; Weiner, S.; Addadi, L. Intracrystalline Macromolecules are Involved in the Morphogenesis of Calcitic Sponge Spicules. *Connect. Tissue Res.* **1996**, *34*, 255–261.
- (14) Killian, C.; Metzler, R.; Gong, Y.; Olson, I.; Aizenberg, J.; Politi, Y.; Wilt, F.; Scholl, A.; Young, A.; Doran, A.; et al. Mechanism of Calcite Co-Orientation in the Sea Urchin Tooth. *J. Am. Chem. Soc.* **2009**, *131*, 18404–18409.
- (15) Politi, Y.; Arad, T.; Klein, E.; Weiner, S.; Addadi, L. Sea Urchin Spine Calcite Forms via a Transient Amorphous Calcium Carbonate Phase. *Science* **2004**, *306*, 1161–1164.
- (16) Killian, C.; Metzler, R.; Gong, Y.; Churchill, T.; Olson, I.; Trubetskoy, V.; Christensen, M.; Fournelle, J.; De Carlo, F.; Cohen, S.; et al. Self-Sharpening Mechanism of the Sea Urchin Tooth. *Adv. Funct. Mater.* **2011**, *21*, 682–690.
- (17) Chien, Y.; Hincke, M.; Vali, H.; McKee, M. Ultrastructural Matrix–Mineral Relationships in Avian Eggshell, and Effects of Osteopontin on Calcite Growth in Vitro. *J. Struct. Biol.* **2008**, *163*, 84–99.
- (18) Fricke, M.; Volkmer, D. Crystallization of Calcium Carbonate Beneath Insoluble Monolayers: Suitable Models of Mineral–Matrix Interactions in Biomineralization? *Top. Curr. Chem.* **2007**, *270*, 1–41.
- (19) Wolf, S.; Leiterer, J.; Pipich, V.; Barrea, R.; Emmerling, F.; Tremel, W. Strong Stabilization of Liquid Amorphous Calcium Carbonate by Ovalbumin: Gaining Insight into the Mechanism of Polymer-Induced Liquid Precursor Processes. *J. Am. Chem. Soc.* **2011**, *133*, 12642–12649.
- (20) Radha, A.; Forbes, T.; Killian, C.; Gilbert, P.; Navrotsky, A. Transformation and Crystallization Energetics of Synthetic and Biogenic Amorphous Calcium Carbonate. *Proc. Natl. Acad. Sci. U.S.A.* **2010**, *107*, 16438–16443.
- (21) Günther, C.; Becker, A.; Wolf, G.; Eppler, M. In Vitro Synthesis and Structural Characterization of Amorphous Calcium Carbonate. *Z. Anorg. Allg. Chem.* **2005**, *631*, 2830–2835.
- (22) Taylor, M.; Simkiss, K.; Greaves, G.; Okazaki, M.; Mann, S. An X-ray Absorption Spectroscopy Study of the Structure and Transformation of Amorphous Calcium Carbonate from Plant Cystoliths. *Proc. Biol. Sci.* **1993**, *252*, 75–80.
- (23) Michel, F.; MacDonald, J.; Feng, J.; Phillips, B.; Ehm, L.; Tarabrella, C.; Parise, J.; Reeder, R. Structural Characteristics of Synthetic Amorphous Calcium Carbonate. *Chem. Mater.* **2008**, *20*, 4720–4728.
- (24) Levi-Kalishman, Y.; Raz, S.; Weiner, S.; Addadi, L.; Sagi, I. Structural Differences between Biogenic Amorphous Calcium Carbonate Phases Using X-ray Absorption Spectroscopy. *Adv. Funct. Mater.* **2002**, *12*, 43–48.
- (25) Levi-Kalishman, Y.; Raz, S.; Weiner, S.; Addadi, L.; Sagi, I. X-ray Absorption Spectroscopy Studies on the Structure of a Biogenic Amorphous Calcium Carbonate Phase. *J. Chem. Soc., Dalton Trans.* **2000**, 3977–3982.
- (26) Hasse, B.; Ehrenberg, H.; Marxen, J.; Becker, W.; Eppler, M. Calcium Carbonate Modifications in the Mineralized Shell of the Freshwater Snail *Biomphalaria glabrata*. *Chem.—Eur. J.* **2000**, *6*, 3679–3685.
- (27) Raz, S.; Hamilton, P.; Wilt, F.; Weiner, S.; Addadi, L. The Transient Phase of Amorphous Calcium Carbonate in Sea Urchin Larval Spicules: The Involvement of Proteins and Magnesium Ions in its Formation and Stabilization. *Adv. Funct. Mater.* **2003**, *13*, 480–486.
- (28) Wagner, W.; Pruss, A. The IAPWS Formulation 1995 for the Thermodynamic Properties of Ordinary Water Substance for General and Scientific Use. *J. Phys. Chem. Ref. Data* **2002**, *31*, 387–536.
- (29) Pipich, V.; Balz, M.; Wolf, S.; Tremel, W.; Schwahn, D. Nucleation and Growth of CaCO₃ Mediated by the Egg-White Protein Ovalbumin: A Time-Resolved *in situ* Study Using Small-Angle Neutron Scattering. *J. Am. Chem. Soc.* **2008**, *130*, 6879–6892.
- (30) Goodwin, A.; Michel, F.; Phillips, B.; Keen, D.; Dove, M.; Reeder, R. Nanoporous Structure and Medium-Range Order in Synthetic Amorphous Calcium Carbonate. *Chem. Mater.* **2010**, *22*, 3197–3205.
- (31) Singer, J. W.; Yazaydin, A. O.; Kirkpatrick, R. J.; Bowers, G. Structure and Transformation of Amorphous Calcium Carbonate: A Solid-State ⁴³Ca NMR and Computational Molecular Dynamics Investigation. *Chem. Mater.* **2012**, *24*, 1828–1836.
- (32) Gebauer, D.; Völkel, A.; Cölfen, H. Stable Prenucleation Calcium Carbonate Clusters. *Science* **2008**, *322*, 1819–1822.
- (33) Meldrum, F.; Sear, R. Now You See Them. *Science* **2008**, *322*, 1802–1803.
- (34) Pouget, E.; Bomans, P.; Goos, J.; Frederik, P.; With, G.; Sommerdijk, N. The Initial Stages of Template-Controlled CaCO₃ Formation Revealed by Cryo-TEM. *Science* **2009**, *323*, 1455–1458.
- (35) Raiteri, P.; Gale, J. D. Water Is the Key to Nonclassical Nucleation of Amorphous Calcium Carbonate. *J. Am. Chem. Soc.* **2010**, *132*, 17623–17634.
- (36) Gale, J.; Raiteri, P.; Van Duin, A. A Reactive Force Field for Aqueous-Calcium Carbonate Systems. *Phys. Chem. Chem. Phys.* **2011**, *13*, 16666–16679.
- (37) Raiteri, P.; Gale, J. D.; Quigley, D.; Rodger, P. M. Derivation of an Accurate Force-Field for Simulating the Growth of Calcium Carbonate from Aqueous Solution: A New Model for the Calcite–Water Interface. *J. Phys. Chem. C* **2010**, *114*, 5997–6010.
- (38) Demichelis, R.; Raiteri, P.; Gale, J.; Quigley, D.; Gebauer, D. Stable Prenucleation Mineral Clusters are Liquid-like Ionic Polymers. *Nat. Commun.* **2011**, *2*, 590.
- (39) Bako, I.; Hutter, J.; Palinkas, G. Car–Parrinello Molecular Dynamics Simulation of the Hydrated Calcium Ion. *J. Chem. Phys.* **2002**, *117*, 9838–9843.
- (40) Tommaso, D.; De Leeuw, N. The Onset of Calcium Carbonate Nucleation: A Density Functional Theory Molecular Dynamics and Hybrid Microsolvation/Continuum Study. *J. Phys. Chem. B* **2008**, *112*, 6965–6975.
- (41) Naor, M. M.; Nostrand, K. V.; Dellago, C. Car–Parrinello Molecular Dynamics Simulation of the Calcium Ion in Liquid Water. *Chem. Phys. Lett.* **2003**, *369*, 159–164.
- (42) Iskrenova-Tchoukova, E.; Kalinichev, A.; Kirkpatrick, R. Metal Cation Complexation with Natural Organic Matter in Aqueous Solutions: Molecular Dynamics Simulations and Potentials of Mean Force. *Langmuir* **2010**, *26*, 15909–15919.
- (43) Smith, W. DL_POLY. *Mol. Simul.* **2006**, *32*, 933–1121.

- (44) Martyna, G.; Klein, M.; Tuckerman, M. Nosé–Hoover Chains: The Canonical Ensemble via Continuous Dynamics. *J. Chem. Phys.* **1992**, *97*, 2635–2643.
- (45) Essmann, U.; Perera, L.; Berkowitz, M.; Darden, T.; Lee, H.; Pedersen, L. A Smooth Particle Mesh Ewald Method. *J. Chem. Phys.* **1995**, *103*, 8577–8593.
- (46) Saharay, M.; Balasubramanian, S. Enhanced Molecular Multipole Moments and Solvent Structure in Supercritical Carbon Dioxide. *ChemPhysChem* **2004**, *5*, 1442–1445.
- (47) Pal, S.; Balasubramanian, S.; Bagchi, B. Identity, Energy, and Environment of Interfacial Water Molecules in a Micellar Solution. *J. Phys. Chem. B* **2003**, *107*, 5194–5202.
- (48) Swainson, I. The Structure of Monohydrocalcite and the Phase Composition of the Beachrock Deposits of Lake Butler and Lake Fellmongery, South Australia. *Am. Miner.* **2008**, *93*, 1014–1018.
- (49) Graf, D. Crystallographic Tables for the Rhombohedral Carbonates. *Am. Miner.* **1961**, *46*, 1283–1316.
- (50) Wang, J.; Becker, U. Structure and Carbonate Orientation of Vaterite (CaCO_3). *Am. Miner.* **2009**, *94*, 380–386.
- (51) Antao, S.; Hassan, I. The Orthorhombic Structure of CaCO_3 , SrCO_3 , PbCO_3 , and BaCO_3 : Linear Structural Trends. *Can. Miner.* **2009**, *47*, 1245–1255.
- (52) Bolze, J.; Peng, B.; Dingenouts, N.; Panine, P.; Narayanan, T.; Ballauff, M. Formation and Growth of Amorphous Colloidal CaCO_3 Precursor Particles as Detected by Time-resolved SAXS. *Langmuir* **2002**, *18*, 8364–8369.
- (53) Liu, J.; Pancera, S.; Boyko, V.; Shukla, A.; Narayanan, T.; Huber, K. Evaluation of the Particle Growth of Amorphous Calcium Carbonate in Water by Means of the Porod Invariant from SAXS. *Langmuir* **2010**, *26*, 17405–17412.
- (54) Faatz, M.; Gröhn, F.; Wegner, G. Amorphous Calcium Carbonate: Synthesis and Potential Intermediate in Biomineralization. *Adv. Mater.* **2004**, *16*, 996–1000.
- (55) Neumann, M.; Epple, M. Monohydrocalcite and Its Relationship to Hydrated Amorphous Calcium Carbonate in Biominerals. *Eur. J. Inorg. Chem.* **2007**, *2007*, 1953–1957.
- (56) Tribello, G.; Bruneval, F.; Liew, C.; Parrinello, M. A Molecular Dynamics Study of the Early Stages of Calcium Carbonate Growth. *J. Phys. Chem. B* **2009**, *113*, 11680–11687.
- (57) Bots, P.; Benning, L.; Rodriguez-Blanco, J.; Roncal-Herrero, T.; Shaw, S. Mechanistic Insights into the Crystallization of Amorphous Calcium Carbonate (ACC). *Cryst. Growth Des.* **2012**, *12*, 3806–3814.
- (58) Smith, D. Molecular Computer Simulations of the Swelling Properties and Interlayer Structure of Cesium Montmorillonite. *Langmuir* **1998**, *14*, 5959–5967.
- (59) Wang, J.; Kalinichev, A.; Kirkpatrick, R.; Hou, X. Molecular Modeling of the Structure and Energetics of Hydrotalcite Hydration. *Chem. Mater.* **2001**, *13*, 145–150.
- (60) Kumar, P.; Kalinichev, A.; Kirkpatrick, R. Hydrogen-Bonding Structure and Dynamics of Aqueous Carbonate Species from Car–Parrinello Molecular Dynamics Simulations. *J. Phys. Chem. B* **2008**, *113*, 794–802.